



Hierarchical porous Cu with high surface area and fluid permeability

Pengcheng Zhu, Zhining Wu, Yuyuan Zhao *

School of Engineering, University of Liverpool, Liverpool L69 3GH, UK

ARTICLE INFO

Article history:

Received 12 June 2019

Received in revised form 12 July 2019

Accepted 12 July 2019

Available online xxxx

Keywords:

Porous material

Nanostructure

Surface

Permeability

ABSTRACT

Surface area and fluid permeability are two key properties of porous metals in many applications. However, it is extremely difficult to achieve both high surface area and fluid permeability in conventional porous metals. In this work, we developed a synergetic manufacturing process by combining space holder and dealloying methods and produced bulk hierarchical porous Cu samples containing micro-pores and nano-pores. The hierarchical porous Cu possesses high electroactive, real and Brunauer–Emmett–Teller surface areas of 0.11, 7.02 and 10.62 m²/g, respectively, a high permeability of 9.5×10^{-10} m² and a low form drag coefficient of 400 m⁻¹.

Porous metals have many applications, e.g., filtration, acoustic absorption, heat management, catalysis, energy generation and storage, due to their unique structures and properties [1–3]. Surface area and fluid permeability of porous metals are key properties particularly important for electrochemical applications. Surface area determines the site size for reaction or charge storage and therefore affects current density and performance [4,5]. High permeability facilitates heat and mass transfer within porous metals [6–8]. Porous metals with both high surface area and permeability are excellent current collectors/catalyst supports in fuel cells [9].

It is extremely difficult to maximize both surface area and permeability of porous metals manufactured by conventional manufacturing processes. Porous metals with milli- and micro-scale pores, produced by loose powder sintering [10], investment casting [11], chemical vapor deposition [12], space holder methods [13,14] or selective laser melting [15], have low surface areas less than 2 m²/g [16–18] and high permeabilities in the range of 10^{-14} – 10^{-9} m² [19–21]. In contrast, porous metals with nanoscale pores, normally produced by chemical dealloying [22–25], provide much higher surface areas up to 10² m²/g [26,27] but very low permeability. In fact, no studies on the fluid permeability of nanoporous metals have been reported in the literature.

Several processes, such as dealloying/plating/redealloying [28], multi-phase precursor dealloying [29,30] and templating/dealloying process [26], can produce multiple-length scale porous metals. However, the large pores produced by these processes are normally smaller than several decades of microns and are rarely controllable.

In this paper, we produced hierarchical porous Cu samples containing both micro- and nano-pores, by combining the Lost Carbonate

Sintering (LCS) method [14] and chemical dealloying for the first time. We measured the surface areas and fluid permeability and studied the effects of dealloying conditions on the nanoporous structure. We compared the hierarchical and micro-porous structures to elucidate the different roles played by the micro- and nano-pores. This study creates a new route for manufacturing hierarchical porous metals with high surface area and good fluid permeability and provides useful insights into the complementary functions of micro- and nano-pores.

The hierarchical porous Cu samples were manufactured by a new process combining LCS and chemical dealloying (Fig. S1). Pure Cu and Zn powders were first mixed at an atomic ratio of 1:1 and further mixed with 50, 60, 70 or 80 vol% of spherical K₂CO₃ powder with a particle size range of 200–450 μm. The mixture was sealed in a cylindrical steel tube, compacted at 200 MPa and sintered at 850 °C for 4 h. The K₂CO₃ particles were subsequently removed by dissolution in water. The obtained samples were cut into different sizes: 20 × 30 × 5 mm³ (for permeability measurements), 5 × 5 × 2.5 mm³ (for surface area measurement) and 5 × 5 × 4.5 mm³ (for thickness effect comparison). The porous CuZn alloy samples were immersed in HCl to dissolve Zn and dried after each dealloying operation. The dealloying parameters were: HCl concentration (5 and 7 M), temperature (20, 35 and 50 °C) and time (0–320 h). For comparison, a non-dealloyed porous Cu (ND Cu) sample containing micro-pores only, with a porosity of 0.80, was manufactured using Cu powder, following the above procedure but without dealloying.

The measurements of electroactive and real surface areas were performed in a three-electrode electrochemical cell using a saturated calomel electrode (SCE) as the reference electrode, a platinum coil as the counter electrode and 0.1 M KOH as the background electrolyte. The electroactive surface area was measured by the cyclic voltammetry peak current method [16,17]. The chemical reaction employed was Cu

* Corresponding author.

E-mail address: yyzhao@liverpool.ac.uk (Y. Zhao).

+ 2OH⁻ → Cu(OH)₂ + 2e, which is controlled by the diffusion of OH⁻ [31,32]. At a scan rate of 0.01 V/s, the electroactive surface area can be calculated by the peak current at a potential of 0.3 V divided by 2.836 A/m² [17]. The real surface area was measured by the cyclic voltammetry double layer capacitance method [16,17] in the potential range of -0.9 to -0.6 V at a scan rate of 0.01 V/s. The BET surface area measurements were conducted in a 3-Flex 3500 gas sorption analyser at 77 K using the nitrogen adsorption method. The samples were degassed at 300 °C under vacuum for 3 h before the measurements.

The permeability and form drag coefficient measurements were conducted in a purpose-built apparatus [7]. The porous sample was inserted in a polytetrafluoroethylene channel and water was forced to flow through the sample. The flow rate of water was measured by a flowmeter with a measurement range of 0.1–1.5 L/min. The inlet and outlet water pressures were measured by two pressure transducers placed in either side of the porous sample. The permeability, K (m²), and form drag coefficient, C (m⁻¹), of the porous samples were determined using the Forchheimer equation [33]:

$$\frac{\Delta P}{L} = \frac{\mu}{K} V + \rho C V^2 \quad (1)$$

where ΔP is the difference between the inlet and outlet water pressures (Pa), L is the length of the porous sample (m), μ is the viscosity of water (8.9×10^{-4} Pa s), ρ is the density of water (997 kg/m³) and V is the Darcian velocity (m/s), which is volume flow rate divided by the cross-sectional area of the porous sample.

The weight of the porous CuZn alloy samples during dealloying decreased nearly linearly with dealloying time until all Zn was dissolved. The times for complete dissolution of Zn under the conditions of 5 M HCl (20 °C), 5 M HCl (35 °C), 5 M HCl (50 °C) and 7 M HCl (20 °C) were 280, 120, 35 and 100 h, respectively. Raising temperature or increasing HCl concentration accelerated the Zn dissolution. Samples with different thicknesses had a similar Zn removal time (Fig. S2). This is because the etchant penetrates the samples through the micro-pores so that the dealloying reaction takes place on both the internal and external surfaces. Thus, sample thickness is no longer a hindrance to the dealloying process and bulk hierarchical nanoporous metals can be manufactured in a short time.

Fig. 1 shows the microstructure of the hierarchical porous Cu sample dealloyed in 5 M HCl at 20 °C for 320 h, with a primary porosity of 0.53 and a secondary porosity of 0.25. The primary porosity is the porosity before dealloying (measured by the Archimedes' method) and the secondary porosity is the porosity formed due to dealloying (calculated from the weight loss). The porous structure consists of interconnected micro-pores (Fig. 1a), which are replicas of the K₂CO₃ particles and have a size of 200–450 μm. The Cu matrix both inside and outside the micro-pores have rough surfaces (Fig. 1b), consisting of numerous nano-sized ligaments and pores (Fig. 1c and d) formed by the dealloying.

Fig. 2 shows the effects of dealloying conditions on the nanoporous structure. The nano-ligament and nano-pore sizes were measured by Image J over 50 sites for each SEM image. The ligament size was taken as the thickness of the remaining Cu ligament, while the nano-pore size was estimated by the shortest distance between the adjacent ligaments. It is obvious that increasing temperature or increasing HCl concentration increases the nano-ligament and nano-pore sizes. In 5 M HCl, the mean nano-ligament and nano-pore sizes increase from 243 and 231 nm to 309 and 250 nm, and further to 367 and 398 nm, as the dealloying temperature was increased from 20 °C to 35 °C and further to 50 °C, respectively. Dealloying in 7 M HCl at 20 °C increased the mean nano-ligament and nano-pore sizes considerably to 464 and 572 nm, respectively.

The changes in the nano-ligament and nano-pore sizes arise from the effects of temperature and etchant concentration on the diffusion rate of Cu. According to the continuum dealloying model proposed by Erlebacher et al. [34], the nano-ligaments and nano-pores are formed due to the aggregation of the more noble element (Cu) by diffusion on the electrolyte/solid interface. Raising dealloying temperature enhances the Cu atomic diffusion and therefore increases the nano-ligament and nano-pore sizes [35,36]. The temperature effect was well demonstrated by the work of Qian and Chen [37] who successfully produced ultrafine nanoporous gold by dealloying at a low temperature. Similarly, increasing HCl concentration can lower the activation energy of Cu diffusion due to chemisorption of chloride ions at the surface, increasing the Cu atomic diffusion rate and therefore coarsening the nano-ligaments and pores [38,39].

The process developed in this work can produce highly controllable hierarchical porous structures. The micro-pore size and primary

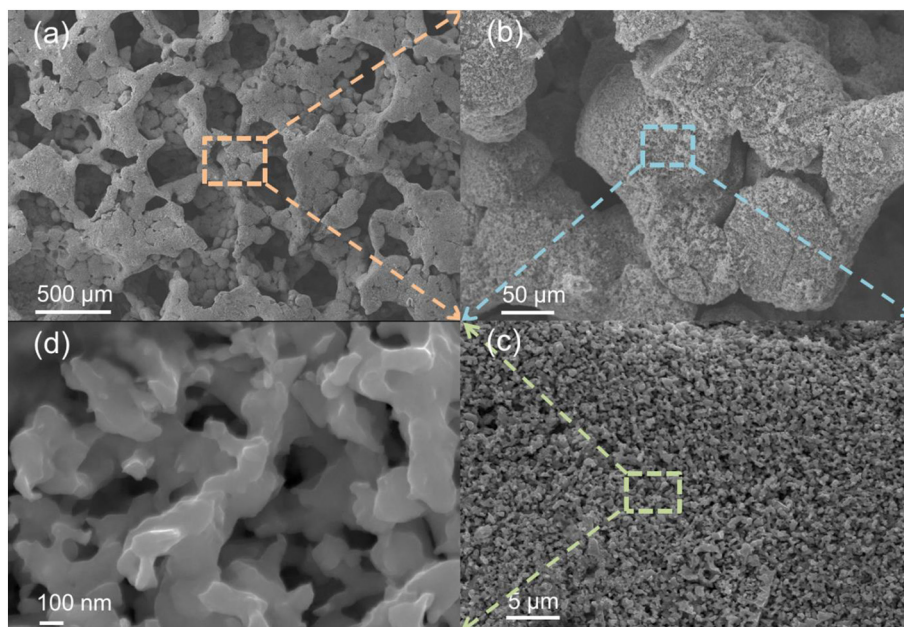


Fig. 1. Microstructure of the hierarchical porous Cu. SEM images of a hierarchical porous Cu sample taken at different magnifications: a) 40, b) 300, c) 3000 and d) 30,000.

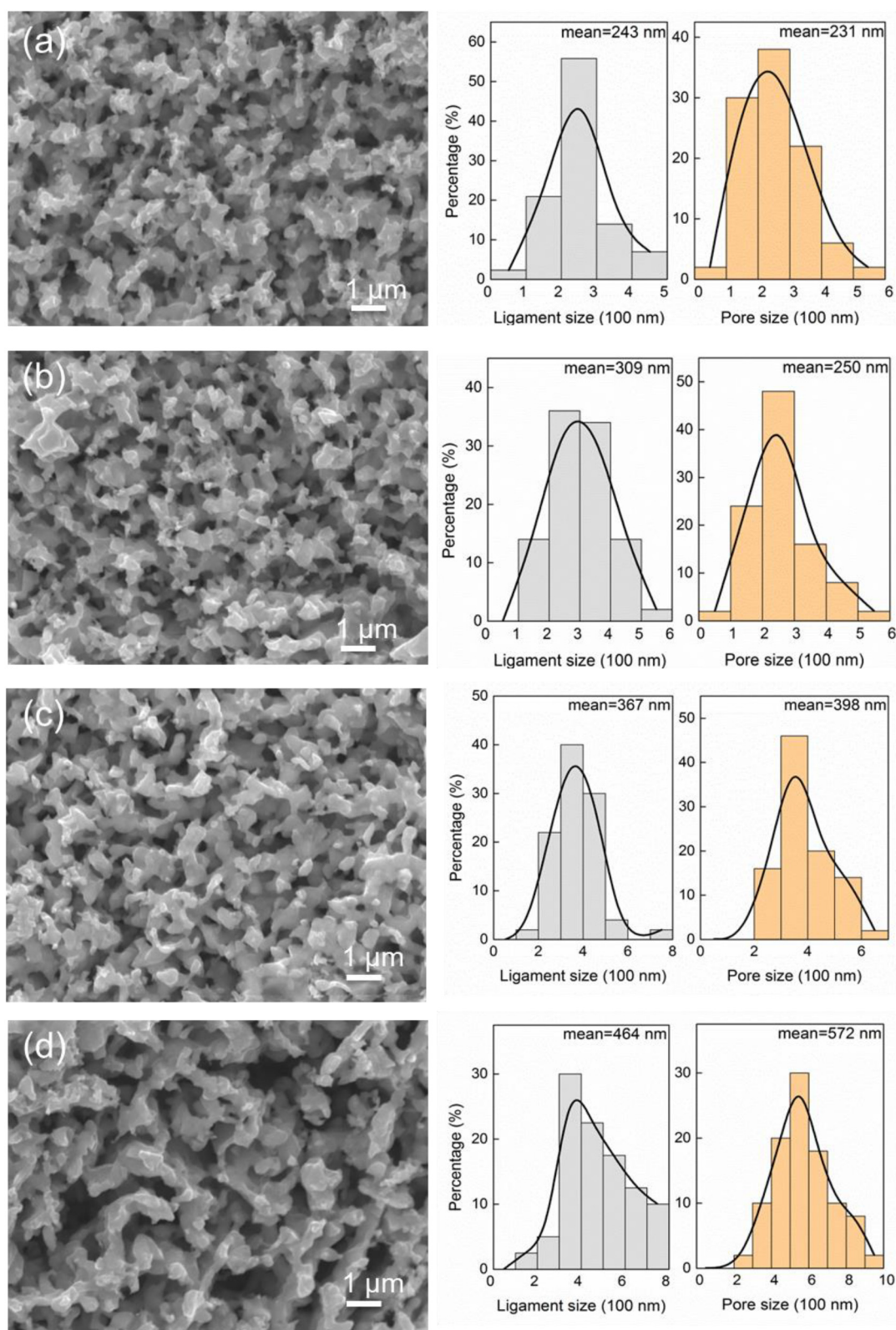


Fig. 2. SEM image (left), nano-ligament size (middle) and nano-pore size (right) distributions of hierarchical porous Cu samples dealloyed under different conditions: a) 5 M HCl at 20 °C, b) 5 M HCl at 35 °C, c) 5 M HCl at 50 °C, and d) 7 M HCl at 20 °C.

porosity can be accurately controlled by selecting the size and amount of the K_2CO_3 particles, while the nano-pore size and secondary porosity can be adjusted by changing the dealloying conditions. Because the LCS process is applicable to many metal systems, including Ni, Cu, Ti, Al and Fe [14], and so does chemical dealloying, e.g., Au–Ag, Au–Al, Pt–Al,

Ni–Al, Ni–Mn and Cu–Al [22,23], the synergetic process can be applied to a wide range of metals and alloys.

Fig. 3a, b and c present the peak current, charge/discharge current and nitrogen absorption used for determining the electroactive, real and BET surface areas, respectively, for the hierarchical porous Cu

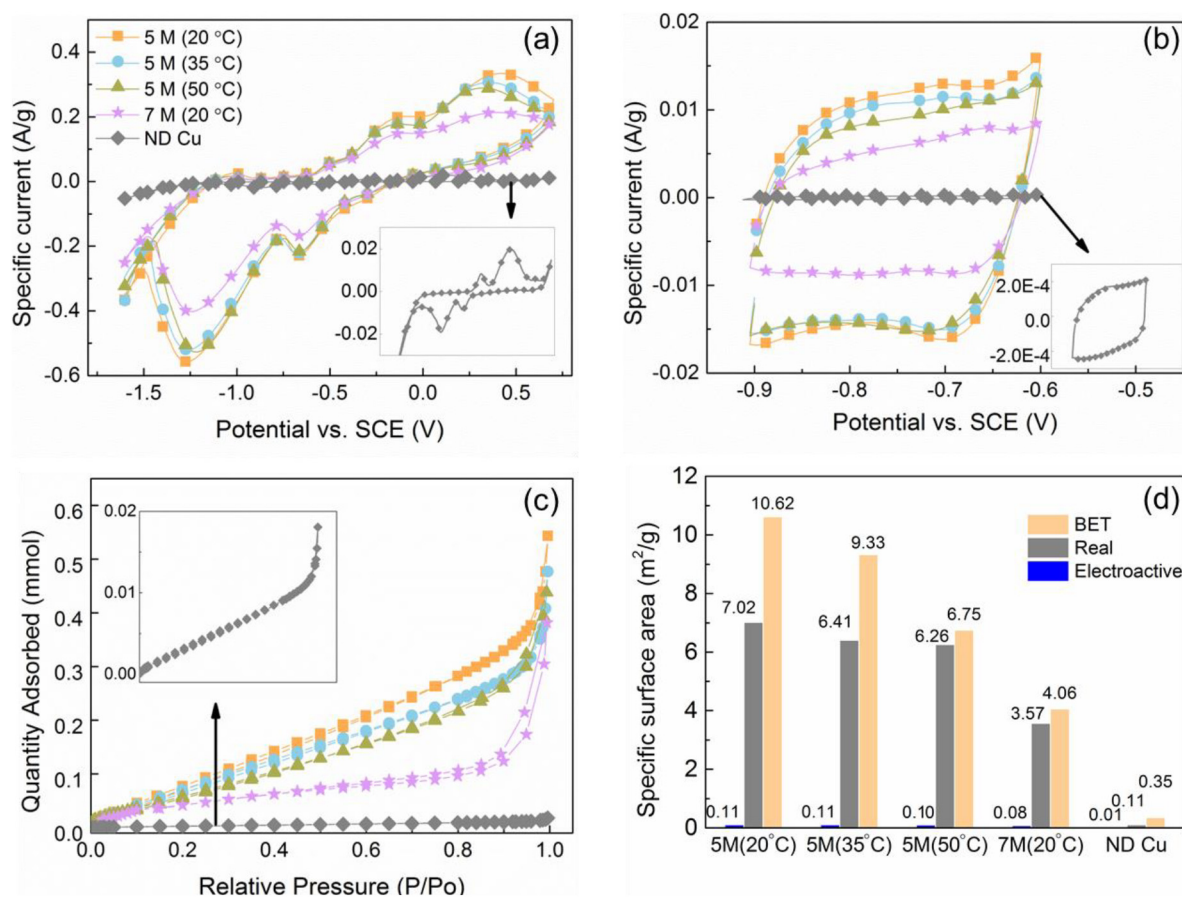


Fig. 3. Electroactive (a), real (b) and BET (c) surface area measurements for the hierarchical porous Cu and ND Cu samples. (d) Comparison of surface areas.

samples with a primary porosity of 0.53 and a secondary porosity of 0.25. These parameters decrease with increasing dealloying temperature or decreasing HCl concentration, indicating negative effects of temperature and HCl concentration on the electroactive, real and BET surface areas. Fig. 3d compares the surface areas of the hierarchical porous Cu under different dealloying conditions, as well as with the ND Cu. In 5 M HCl, the electroactive, real, BET surface areas of the hierarchical porous Cu dealloyed at 20 °C are 0.11, 7.02, 10.62 m²/g, respectively. As the temperature was increased to 35 °C and further to 50 °C, the electroactive, real, BET surface areas decreased to 0.11, 6.41, 9.33 m²/g and further to 0.10, 6.26, 6.75 m²/g, respectively. Increasing dealloying temperature from 20 to 50 °C decreases the electroactive, real and BET surface areas by about 9%, 11% and 30%, respectively. The effects of HCl concentration on the surface areas are even stronger. Increasing HCl concentration from 5 to 7 M, at the same dealloying temperature of 20 °C, decreases the electroactive, real and BET surface areas by 30%, 50% and 60%, respectively. The effects of dealloying temperature and etchant concentration on surface areas can be attributed to the changes in the nano-ligament and nano-pore sizes. A higher dealloying temperature or HCl concentration results in a larger nano-ligament size and a larger nano-pore size (Fig. 2), which lead to lower surface areas, especially the real and BET ones.

For comparison, the electroactive, real and BET surface areas of the ND Cu are 0.01, 0.11 and 0.35 m²/g, respectively (Fig. 3d). It means that the electroactive, real and BET surface areas of the hierarchical porous Cu samples are up to 11, 60 and 30 times of those of the ND Cu sample with a similar total porosity, indicating that the surface area increments mainly come from the secondary porosity (nano-pores) rather than the primary porosity (micro-pores). It is also interesting to note that the real surface area is 45–60 times of the electroactive surface area for the hierarchical porous Cu samples, compared to 11 times for

LCS porous Cu samples containing micro-pores only [16,17]. This means that nano-pores have a stronger enhancing effect on the real surface area that is at a smaller length scale than the electroactive surface area that is at a larger length scale.

Fig. 4a plots the length-normalised pressure drop ($\Delta P/L$) as a function of Darcian flow velocity (V) for four porous CuZn samples, with primary porosities of 0.53, 0.62, 0.73 and 0.82, after different dealloying times of 0, 40, 80 and 120 h in 5 M HCl at 35 °C. For each primary porosity, increasing dealloying time results in increases in the secondary porosity and the total porosity. At the same flow velocity, the length-normalised pressure decreases rapidly with increasing primary porosity and dealloying time, indicating that both primary and secondary porosities can make the sample more permeable.

Fig. 4b and c show the permeability and form drag coefficient of the four porous CuZn samples after different dealloying times as a function of total porosity, obtained by fitting the plots in Fig. 4a to Eq. (1). Although increasing total porosity generally increases permeability and decreases form drag coefficient, it is clear that primary and secondary porosities have considerably different degrees of effect. The permeability of the non-dealloyed samples, where the total porosity is equal to the primary porosity, increases exponentially and the form drag coefficient decreases exponentially with increasing porosity, in agreement with the literature [19,40]. For any sample, the permeability increases and the form drag coefficient generally decreases with increasing dealloying time, i.e., with increasing secondary porosity. However, the effects of increasing secondary porosity on the permeability and form drag coefficient are much less than those of increasing primary porosity. Take the sample with a primary porosity of 0.53 as an example. Complete dealloying for 120 h generates a secondary porosity of 0.25, resulting in a total porosity of 0.78. The permeability increases from 6.69×10^{-11} to 9.37×10^{-11} m², i.e., by 40%, while the form drag coefficient

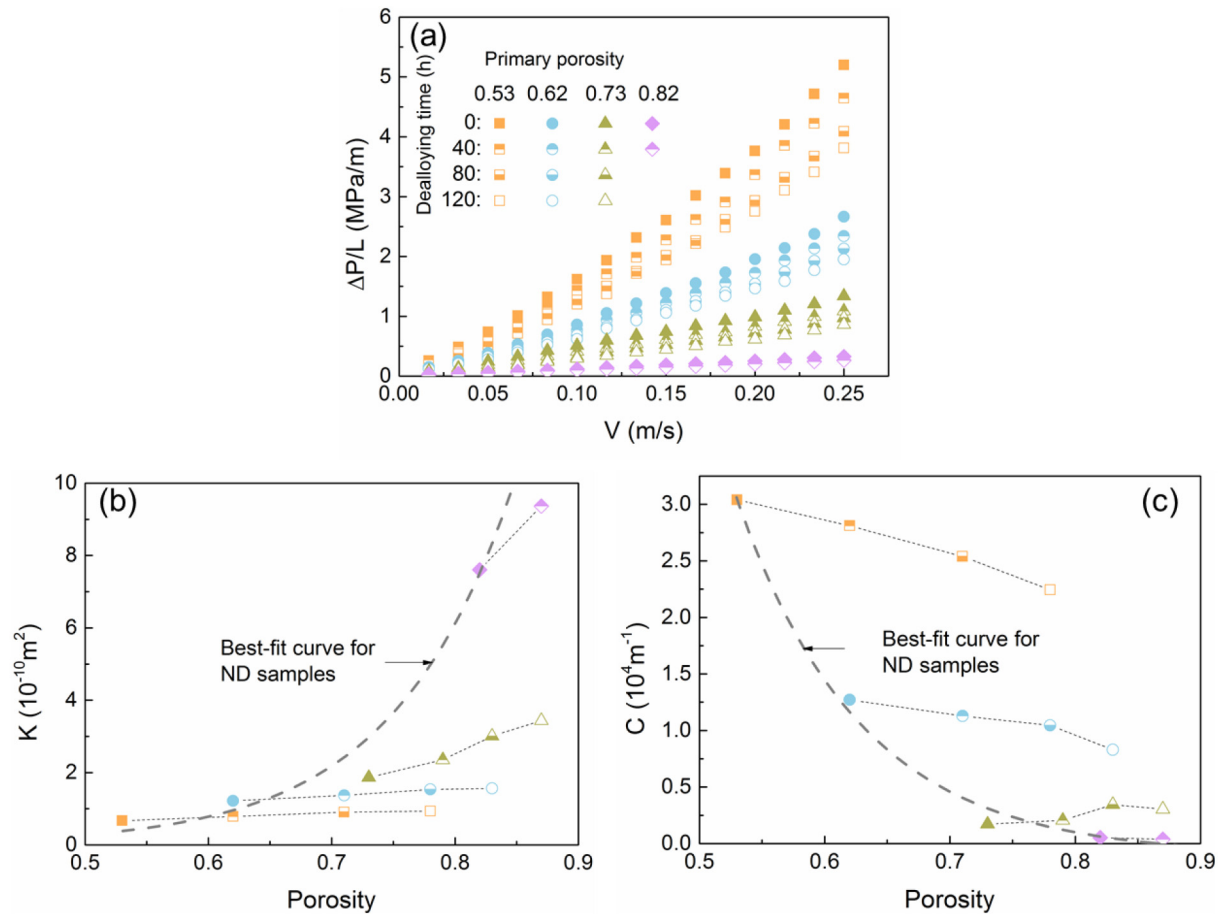


Fig. 4. a) Length-normalised pressure drop ($\Delta P/L$) versus Darcian flow velocity (V) curves for four porous CuZn samples after different dealloying times. b) Permeability and c) form drag coefficient of these samples, obtained from graph a, as a function of total porosity. Note: the sample with a primary porosity of 0.82 was only measured before dealloying and after dealloying for 40 h because the structure after further dealloying was too fragile to stand the fluid pressure.

decreases from 3.04×10^4 to $2.24 \times 10^4 \text{ m}^{-1}$, i.e., by 26%. Increasing the primary porosity from 0.53 to 0.78, the permeability would increase to $4.5 \times 10^{-10} \text{ m}^2$ (by 570%) and the form drag coefficient would decrease to $0.3 \times 10^4 \text{ m}^{-1}$ (by 90%), as estimated from the fitted K and C curves in Figs. 4b and c. In other words, for the same porosity increment of 0.25, the efficiency of the secondary porosity is about 7% of the primary porosity for permeability and 30% for form drag coefficient. This difference is understandable, because nano-pores exert greater friction and resistance to the fluid flow than micro-pores.

It is worth noting that the degrees of the effect of secondary porosity on permeability and form drag coefficient are different and are also dependent on the primary porosity. At a low primary porosity (e.g. 0.53), increasing secondary porosity increases permeability only slightly but decreases form drag coefficient markedly. At a high primary porosity (e.g. 0.73), increasing secondary porosity increases permeability more noticeably but has little effect on form drag coefficient.

In summary, bulk hierarchical porous Cu containing both micro- (200–450 μm) and nano-pores (200–600 nm) has been produced successfully by a newly-developed synergetic manufacturing process combining Lost Carbonate Sintering and chemical dealloying. The hierarchical porous Cu has high electroactive, real and BET surface areas of 0.11, 7.02 and 10.62 m^2/g , respectively, which are up to 60 times higher than a conventional porous Cu containing only micro-pores. The hierarchical porous Cu has a permeability of 6.5×10^{-11} – $9.5 \times 10^{-10} \text{ m}^2$ and a form drag coefficient of 400–30,000 m^{-1} , mainly due to the micro-pores. The contributions of nano-pores to permeability and form drag coefficient are only about 7% and 30%, respectively, of those of the micro-pores.

Funding

This work was supported by an IAA award as further funding from the Engineering and Physical Sciences Research Council, UK (Grant No. EP/N006550/1).

Declaration of Competing Interest

None.

Acknowledgment

The authors would like to thank Mr. Zejun Wang for his help in sample preparation.

Appendix A. Supplementary data

Supplementary data to this article can be found online at <https://doi.org/10.1016/j.scriptamat.2019.07.019>.

References

- [1] M.F. Ashby, T. Evans, N.A. Fleck, J. Hutchinson, H. Wadley, L. Gibson, *Metal Foams: A Design Guide*, Butterworth-Heinemann, Boston, 2000.
- [2] J. Banhart, *Prog. Mater. Sci.* 46 (2001) 559–632.
- [3] L.P. Lefebvre, J. Banhart, D.C. Dunand, *Adv. Eng. Mater.* 10 (2008) 775–787.
- [4] A.J. Bard, L.R. Faulkner, *Electrochemical Methods: Fundamentals and Applications*, second ed. John Wiley & Sons, New York, 2001.
- [5] P. Zhu, Y. Zhao, *Mater. Chem. Phys.* 233 (2019) 60–67.
- [6] P. Zhu, Y. Zhao, *Adv. Eng. Mater.* 19 (2017) 1700392.
- [7] Z. Xiao, Y. Zhao, *J. Mater. Res.* 28 (2013) 2545–2553.

- [8] J.M. Baloyo, Y. Zhao, MRS Proc. 1779 (2015) 39–44.
- [9] W. Yuan, Y. Tang, X. Yang, Z. Wan, Appl. Energy 94 (2012) 309–329.
- [10] Y. Torres, S. Lascano, J. Bris, J. Pavón, J.A. Rodríguez, Mater. Sci. Eng. C 37 (2014) 148–155.
- [11] C. Hintz, I. Wagner, P. Sahm, P. Stoyanov, in: J. Banhart, M.F. Ashby, N.A. Fleck (Eds.), Metal Foams and Porous Metal Structures, MIT-Verlag, Bremen 1999, pp. 153–158.
- [12] V. Paserin, S. Marcuson, J. Shu, D.S. Wilkinson, Adv. Eng. Mater. 6 (2004) 454–459.
- [13] Y. Zhao, D. Sun, Scr. Mater. 44 (2001) 105–110.
- [14] Y. Zhao, T. Fung, L. Zhang, F. Zhang, Scr. Mater. 52 (2005) 295–298.
- [15] Z. Sun, X. Tan, S.B. Tor, W.Y. Yeong, Mater. Des. 104 (2016) 197–204.
- [16] K.K. Diao, Z. Xiao, Y.Y. Zhao, Mater. Chem. Phys. 162 (2015) 571–579.
- [17] P. Zhu, Y. Zhao, RSC Adv. 7 (2017) 26392–26400.
- [18] A. Đukić, V. Alar, M. Firak, S. Jakovljević, J. Alloys Compd. 573 (2013) 128–132.
- [19] J.F. Despois, A. Mortensen, Acta Mater. 53 (2005) 1381–1388.
- [20] C. Zhang, J.W. Palko, G. Rong, K.S. Pringle, M.T. Barako, T.J. Dusseault, M. Asheghi, J.G. Santiago, K.E. Goodson, ACS Appl. Mater. Interfaces 10 (2018) 30487–30494.
- [21] A. Otaru, A.R. Kennedy, Scr. Mater. 124 (2016) 30–33.
- [22] Z. Zhang, Y. Wang, Z. Qi, W. Zhang, J. Qin, J. Frenzel, J. Phys. Chem. C 113 (2009) 12629–12636.
- [23] T. Song, M. Yan, M. Qian, Corros. Sci. 134 (2018) 78–98.
- [24] N.T. Tuan, J. Park, J. Lee, J. Gwak, D. Lee, Corros. Sci. 80 (2014) 7–11.
- [25] G.G. Li, E. Villarreal, Q. Zhang, T. Zheng, J.-J. Zhu, H. Wang, ACS Appl. Mater. Interfaces 8 (2016) 23920–23931.
- [26] T. Fujita, Y. Kanoko, Y. Ito, L. Chen, A. Hirata, H. Kashani, O. Iwatsu, M. Chen, Adv. Sci. 2 (2015) 1500086.
- [27] J. Biener, A. Wittstock, L. Zepeda-Ruiz, M. Biener, V. Zielasek, D. Kramer, R. Viswanath, J. Weissmüller, M. Bäumer, A. Hamza, Nat. Mater. 8 (2009) 47–51.
- [28] Y. Ding, J. Erlebacher, JACS 125 (2003) 7772–7773.
- [29] E. Detsi, S. Punzhin, J. Rao, P.R. Onck, J.T.M. De Hosson, ACS Nano 6 (2012) 3734–3744.
- [30] E. Detsi, S.H. Tolbert, S. Punzhin, J.T.M. De Hosson, J. Mater. Sci. 51 (2016) 615–634.
- [31] N. Hampson, J. Lee, K. Macdonald, J. Electroanal. Chem. Interfacial Electrochem. 34 (1972) 91–99.
- [32] J. Ambrose, R. Barradas, D. Shoesmith, J. Electroanal. Chem. Interfacial Electrochem. 47 (1973) 47–64.
- [33] E.A. Moreira, M.D.M. Innocentini, J.R. Coury, J. Eur. Ceram. Soc. 24 (2004) 3209–3218.
- [34] J. Erlebacher, M.J. Aziz, A. Karma, N. Dimitrov, K. Sieradzki, Nature 410 (2001) 450–453.
- [35] W. Liu, S. Zhang, N. Li, J. Zheng, Y. Xing, Microporous Mesoporous Mater. 138 (2011) 1–7.
- [36] Z. Dan, F. Qin, S. Yamaura, Y. Sugawara, I. Muto, N. Hara, J. Alloys Compd. 581 (2013) 567–572.
- [37] L. Qian, M. Chen, Appl. Phys. Lett. 91 (2007), 083105.
- [38] F. Delamare, G. Rhead, Surf. Sci. 28 (1971) 267–284.
- [39] H. Martin, P. Carro, A. Hernández Creus, J. Morales, G. Fernandez, P. Esparza, S. Gonzalez, R. Salvarezza, A. Arvia, J. Phys. Chem. B 104 (2000) 8229–8237.
- [40] J.M. Baloyo, Porous metals with novel structures for optimum heat exchange performance, PhD thesis, University of Liverpool (2016), pp. 88–89.